Mathematical Biology & Bioinformatics. 2010. V. 5. № 2. P. 176–187.
URL: http://www.matbio.org/downloads_en/Ustinin2010(5_176).pdf

========== **MATHEMATICAL MODELING** ==========

UDC: 612.825.5+004.925

Kinematic visualization of human magnetic encephalography

Ustinin M.N. [1*], Kronberg E.[2], Filippov S.V.[1], Sychev V.V.[1], Sobolev E.V.[1], and Llinás R.[2]

[1]*Institute of Mathematical Problems of Biology RAS, Pushchino, 142290, Russia*
[2]*New York University School of Medicine, New York, NY 10016, USA*

Abstract. A method is presented for the analysis of magneto-encephalographic (MEG) data from a cognitive study involving auditory activity in humans. Signal averaging based on the moment of stimulus onset was used to extract the evoked magnetic field from the spontaneous activity. Positions and dipole moment estimation for auditory sources i.e. "the inverse problem" was addressed for each time point in the interstimulus interval. Two field-map sequences were generated, one corresponding to the direct magnetic field responses over the head and the other to the inverse-problem solutions and software developed for simultaneously field map superposition (SFMS). SFMS, included whole-head tomography, stimulus time series, auditory evoked fields and inverse-problem solutions. A computer movie was created to provide an accessible overview of magnetic-encephalography methods and to demonstrate its application to auditory research. The methods and software developed are applicable to other MEG recording sets.

Keywords: *magnetic encephalography, auditory activity, evoked magnetic fields, voxel model, rendering, composing.*

INTRODUCTION

Magnetic encephalography (MEG) was developed in order to address brain function using the magnetic fields associated with current flow in brains neuronal circuits. In principle giving the lack of magnetic fields distortion by the brain and cranial tissues such recording should allow the location and time distribution of the elementary current dipoles that evoked these fields. Magnetic encephalographs rely on as the high sensitivity of superconductive quantum-interference devices (SQUIDS) to measurement the weak magnetic fields flowing across the head's surface, with high precision. A great number of recording channels (several hundred) and a high registration frequency (several hundred Hz) provide a rather broad and considerably detailed space-time picture of the field representing the underlying electrical activity of the brain. However, the analysis of such activity must consider that the brain addresses many sensory-motor parameters in parallel. As a result, the integrated electrical activity of the brain at each point in space and time is complex, making it necessary to attempt unraveling the individual functional component as separable entities.

This unraveling of the distinct spatiotemporal components requires that the inverse problem be addressed, namely, reconstructing the arrangement of the field sources in time and 3D space, as determined by a functional coordinate geometry. The results of this calculation are functionally meaningful only if they can be correlated to anatomic information concerning the brain being studied. Thus, a complete set of measurements must include, in addition to

* ustinin@impb.psn.ru

magnetic recordings, morphological data, obtained from co-registered MRI tomography. The purpose of this work was to develop methods and software to analyze and integrally represent the results of magnetoencephalography/morphology data. To this purpose we developed an integrated software system capable of dynamic visualization of the results using a computer graphics program.

Towards this aim MEG data obtained with a 148-magnetometer coil system (Magnes 2500 WH) was assembled from auditory evoked recordings performed at Bellevue Hospital at New York University Medical School Center for Neuromagnetism [1]. The SQUID-based magnetic-field detectors immersed in a Dewar of liquid helium. The coils are 2.3 cm in diameter, and the average distance between the centers of the coils was approximately 2.9 cm. The sensors were embedded in a helmet fixed at the bottom of the Dewar and distributed equidistantly over the entire surface of the subject's head. The auditory stimuli were presented at a frequency of 7.3825 Hz into the left ear of a healthy human volunteer.

ANALYSIS OF EXPERIMENTAL DATA

Because evoked fields are an order of magnitude weaker than spontaneous activity, the evoked fields were filtered by averaging the data over reference points. This approach has proven useful and efficient by a widely used set of MEG centers around the world. [2, 3]

The basic algorithm developed for SFMS . Makes the fundamental assumption that the recorded magnetic signal represent, the spatial-temporal sequence of the magnetic fields $m(t,k)$ resulting from the brain's response to the auditory stimulus. Here, $m(t,k)$ is a magnetic field measured by the *k*th sensor at time *t*, $k = 1,\ldots,K$, *K* is the total number of sensors (registration channels) and $t = t_1,\ldots,t_n$, $(t_1 - t_n)$ is the duration of the useful signal, for example, the interval between the moments of similar stimulus onsets.

Noise is defined as $\chi(t,k)$: i.e. all brain activity that is unrelated to the stimulus. It is also assumed that the signal and the noise are additive; Thus the MEG fields recorded during the duration of the response was written as $m(t,k)+\chi(t,k)$, Note that $m(t,k)$ is constantly repeated as a reaction to each response and that the quantity $\chi(t,k)$ is random. After multiple repetitions of a stimulus (nearly 2,000 times) and its co-registration in time the signal was filtered out by averaging;

$$m(t_i,k)+\overline{\chi}(t_i,k)=\frac{1}{L}\sum_{l=1}^{L}m(t_{li},k)+\frac{1}{L}\sum_{l=1}^{L}\chi(t_{li},k),$$

where t_{li} is the *i*-th point of the duration of a response to the *l*-th stimulus, t_{l1} is the *l*-th reference point used for averaging, *k* is the channel number, $i = 1,\ldots,n$ – sample number in auditory response. The reference points used for averaging t_{l1} were taken from the stimulus records made during the experiment, each determined as the moment of stimulus onset. By averaging, we extracted an auditory response to the stimulus $\overline{m}(t_i,k)=m(t_i,k)+\overline{\chi}(t_i,k)$. This signal still contained a residual noise component (approximately 20%), but the signal-to-noise ratio was improved by a $\sqrt{L}$ factor, which allowed us to address the inverse problem. The next step related to the actual analysis and visualization of the averaged response $\overline{m}(t_i,k)$.

The filtering and analysis of the MEG data was implemented via the integrated software system MRIAN [4, 5]. Fig. 1 shows a working window of the software, displaying an averaged response to an auditory stimulus. As indicated, the response has two main maxima: at 65 and 129 ms following the stimulus onset. Giving conduction time to cortical level we interpreted the onset of the magnetic field peak to be similar to the M50 (the analog of PI peak in the EEG), which is the magnetic component of the response to the onset of the auditory stimulus, arising 50 ms after the stimulus. It is assumed that second peak is also part of the response generated in this case by, the termination (off response) of the stimulus after

one-half period. The other components of the auditory response, including the main peak M100 (the analog of the peak N1 in the EEG), were not observed due to the high frequency of the stimulus pattern.

The effect of smoothing the N1 peak at frequencies close to the experimental ones has been reported in a previous study [2]. Additionally, in our experiment the stimulus duration was equal to the duration of the pause before the onset of the next stimulus; according to the model suggested in [6] peak M100 disappears at any interval between the stimuli.

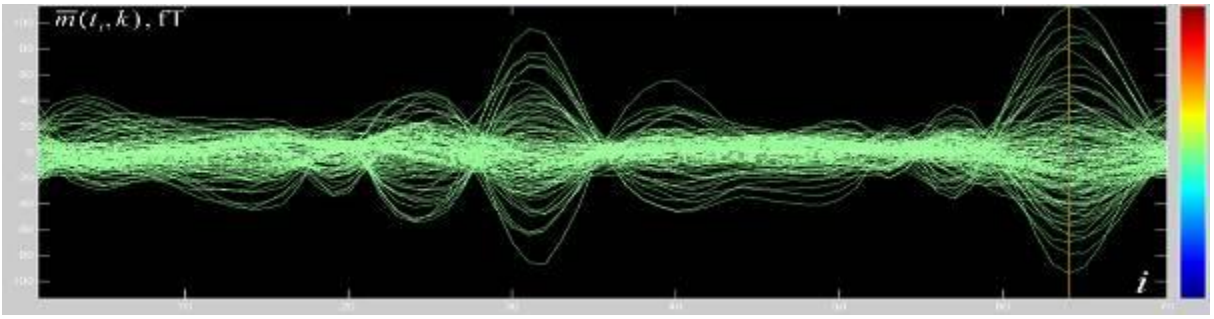

Fig. 1. Magnetoencephalography of an auditory response filtered off by averaging over the moments of stimulus onset. 148 registration channels at 70 points taken at increments of 2 ms are shown. The vertical line marks the 128 ms instant of time chosen for mapping and solving the inverse problem (see Fig.2). On the right is a color scale establishing a correspondence between the color on the amplitude map of Fig.2 and the field intensity.

SOLUTION OF THE INVERSE PROBLEM

Using the MRIAN system [4, 5], we addressed the encephalographic inverse problem for each time point of the averaged signal. To perform this calculation, we minimized the root-mean-square deviation between the model and the experimental values of the magnetic induction

$$\sum_{k=1}^{K} \left(B_k - B_k^0\right)^2 \to \min .$$

Here, $B_k^0 = \overline{m}(t_i, k)$ is the magnetic induction measured by the kth sensor at time t_i, and $B_k = \left(\mathbf{B}(\mathbf{r}_k), \mathbf{n}_k\right)$ is the induction of the model field calculated for the position of the kth sensor $\mathbf{r}_k$ and its direction $\mathbf{n}_k$. The sources of auditory activity were simulated here using two equivalent current dipoles. The induction $\mathbf{B}(\mathbf{r}_k)$ was calculated as the sum of two magnetic dipoles, each described by the model of a current dipole inside a conducting sphere [7]:

$$U(\mathbf{r}) = -\frac{1}{4\pi}\frac{(\mathbf{Q}\times\mathbf{r}_0, \mathbf{r})}{F}$$

$$F = a\left(ar + r^2 - (\mathbf{r}_0, \mathbf{r})\right), \quad \mathbf{a} = \mathbf{r} - \mathbf{r}_0, \quad \mu_0 = 4\pi\cdot 10^{-7}.$$

Minimization with respect to the dipole positions was performed using a Nelder-Mead simplex method [8], whereas minimization with respect to the dipole moment at a fixed position of the dipole was calculated by solving a system of linear equations, as the magnetic induction depends linearly on the dipole moment. Thus, each trial calculation depended on two vector parameters, i.e., the positions of two dipoles.

We used amplitude mapping to image the magnetic-field pattern at each time point. The spatial positions of the sensors were projected onto the plane and then a two-dimensional interpolation of the sensor readings on a nonuniform grid was performed [9] using biharmonic interpolation splines $B(\mathbf{x})$ passing through the specified points $B(\mathbf{x}_j) = B_j$ and satisfying the biharmonic equation:

$$\mathbf{\Delta}^2 B(\mathbf{x}) = \sum_{k=1}^{K} \alpha_k \delta(\mathbf{x} - \mathbf{x}_k),$$

where $\mathbf{\Delta}$ is Laplace operator, δ is Dirac delta function, $\mathbf{x} \in \mathbf{R}^2$, $\mathbf{x}_j$ are positions of magnetic sensors on the surface, $\mathbf{x}_k$ is a new grid.

For mapping, we used a general solution of the equation $B(\mathbf{x}) = \sum_{k=1}^{K} \alpha_k \varphi(\mathbf{x} - \mathbf{x}_k)$, where coefficients α_k were found by solving the system of linear equations $B_j = \sum_{k=1}^{K} \alpha_k \varphi(\mathbf{x}_j - \mathbf{x}_k)$, the biharmonic Green function $\varphi(\mathbf{x})$ had the form $\varphi(\mathbf{x}) = |\mathbf{x}|^2 \cdot (\ln|\mathbf{x}| - 1)$ in the two-dimensional case.

So, at each instant of time t two amplitude maps of the magnetic field were constructed: one corresponding to the experimental encephalogram and the other corresponding to the model field, i.e., the inverse-problem solutions.

To study the spatial distribution of the electrical activity sources of the brain, a T1-weighted nuclear-magnetic-resonance (NMR) tomogram was taken at increments of 1 mm in all three dimensions. An NMR tomogram is acalar function of three spatial variables that represents the brain structure with a degree of completeness that is sufficient for localization.

In Fig. 2 a working window of the MRIAN system is illustrated, which displays an NMR tomogram, an experimental magnetic field, the inverse-problem solutions (dipole coordinates and directions) and the magnetic field calculated from these dipoles.

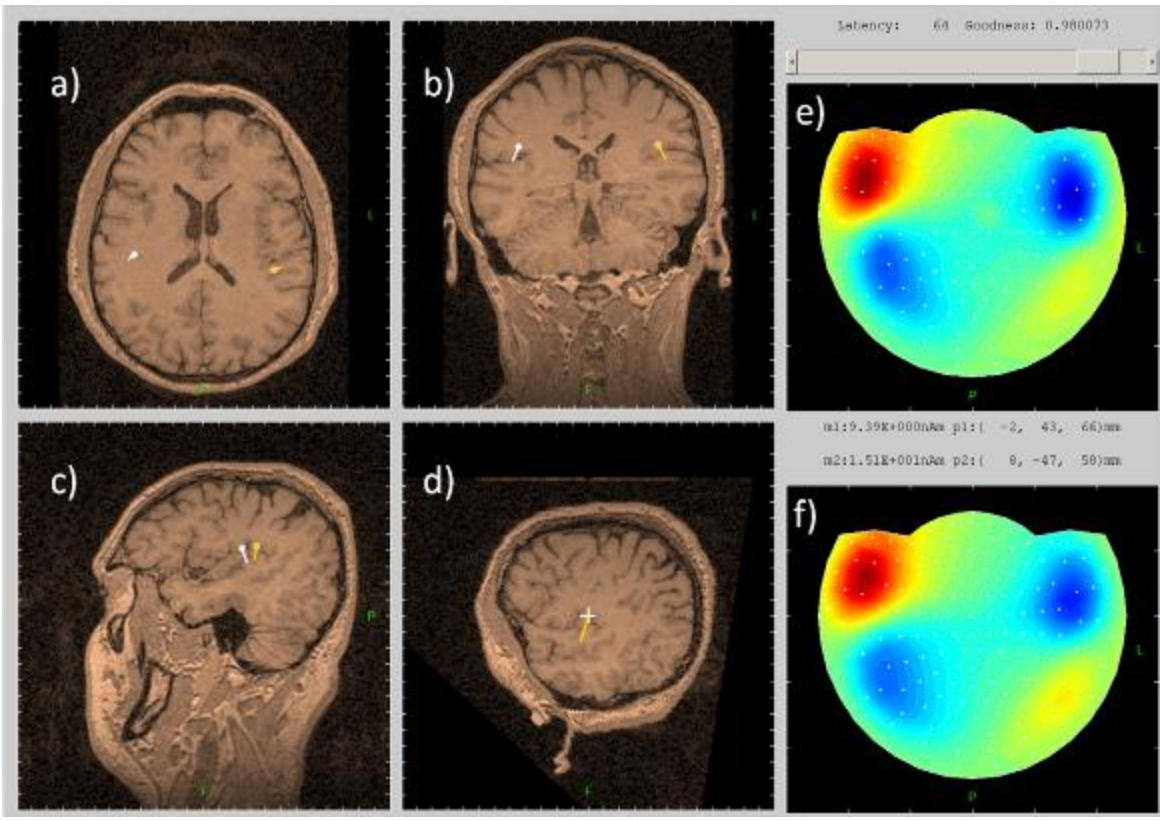

Fig. 2. Solution of the inverse problem for the auditory response magnetoencephalogram at the moment of maximum (see Fig.1) found with the use of the model of two current dipoles. Windows a) – c) Standard tomographic sections passing through a dipole marked in yellow; window d) Tangential section of the tomogram through the same dipole; window e) Experimental magnetic field; window f) Calculated magnetic field induced by model dipoles.

Note that the representation of the tomogram as a set of sections passing through a dipole provides a complete image of its position in the brain. Of special significance here is the tangential section, orthogonal to the radial vector, connecting the model dipole with the center of the conducting sphere within which the inverse problem is solved. As indicated by Formula (1), the MEG records only the dipole-induced field with a moment lying in the tangential-section plane. Window (d) illustrates the anatomic justification of the inverse-problem solution.

The working windows of the system shown in Figs. 1 and 2 enable the user to work simultaneously with both the experimental and calculated magnetic-resonance tomography and magnetic-encephalography data. However, the data sets are bulky spatial-temporal objects that cannot be viewed in their entirety using the computational program. This problem arises in the many modern scientific applications involving abundant data and complicated mathematical models. We attempted to solve the problem using the powerful capabilities of a commercial image-compositing software package.

Visualization of the magnetoresonance tomogram

The tomogram is, thus, presented as a discrete scalar function of three variables with 1-mm spacing over three dimensions. Methods for visualizing 3D functions that match each point with a corresponding geometric primitive, such as a semitransparent cube [10] or a cloud of points, are no longer used, as they do not ensure a high-quality model presentation and have the disadvantage of being computationally complex. Methods for presenting 3D data using isosurfaces [11, 12] can solve the problem of binary classification but yield false-positive (false surfaces) and false-negative (erroneous holes in the surface) solutions. Additionally, isosurfaces neglect information; therefore, other methods are better suited to study the general form of the tomogram, whereas isosurfaces and sections are more appropriate for the treatment of local peculiarities. A 3D data projection can be obtained by addressing a stack of semitransparent parallel planes of the imaged tomogram sections [13]. This approach is used in hardware accelerators and cannot easily be optimized or modified. In the present paper, we describe a method based on direct projection of the volume [14, 15] with some modifications, as described below. The method produces a high-quality image and performs some additional processing while calculating the projection and is easily modified so that the general scene, which also contains some geometrical objects, can be calculated. Moreover, the procedure fits into the general backward-ray-tracing algorithm of any other computer-graphics software.

We consider a 3D function as a medium with varying optical density [16]. The loss of intensity of the projecting beam is greater when it passes through the denser regions of the medium than through the rarefied ones. The color can also depend on the density of the medium. The resulting projection of such a medium conveys cumulative information on the function gathered during beam penetration.

Let us consider briefly the algorithm for the visualization of scientific data. The function is given by a data array in which each three-digit group of discrete coordinates corresponds to a scalar value:

$$\langle u,v,w\rangle \to f_i, \quad u,v,w \text{ - целые : } 0 \le u < n_x, 0 \le v < n_y, 0 \le w < n_z .$$

First, we construct a texture map, which is a parallelepiped restricting the region of space onto which the function is mapped (see Fig.3a). An arbitrary bounded polyhedron *S* (with which the texture map is associated) specifies the region within the general scene where the function will be visualized.

The essence of the algorithm is to determine the total influence of the function to be visualized on the beam visible to the user. The function is presented as a bulky optical entity, with function values that determine the optical density at each point. The data is integrated

along beam penetration from one face of polyhedron *S* to another, with spacing approximately equal to the discrete increment of the function. As a result, the medium is divided into thin layers perpendicular to the beam (see Fig. 3b). The aim of the algorithm is to determine the color $\vec{C} = (r, g, b)$ and intensity I of the beam after it reaches the nearest boundary of polyhedron *S*. For visualization purposes, it is assumed that each layer is partially transparent; in other words, the layer allows the beam to pass but diminishes its intensity (Fig. 3c). Each decrease in beam intensity reduces the influence of the layer on the resulting color of the beam.

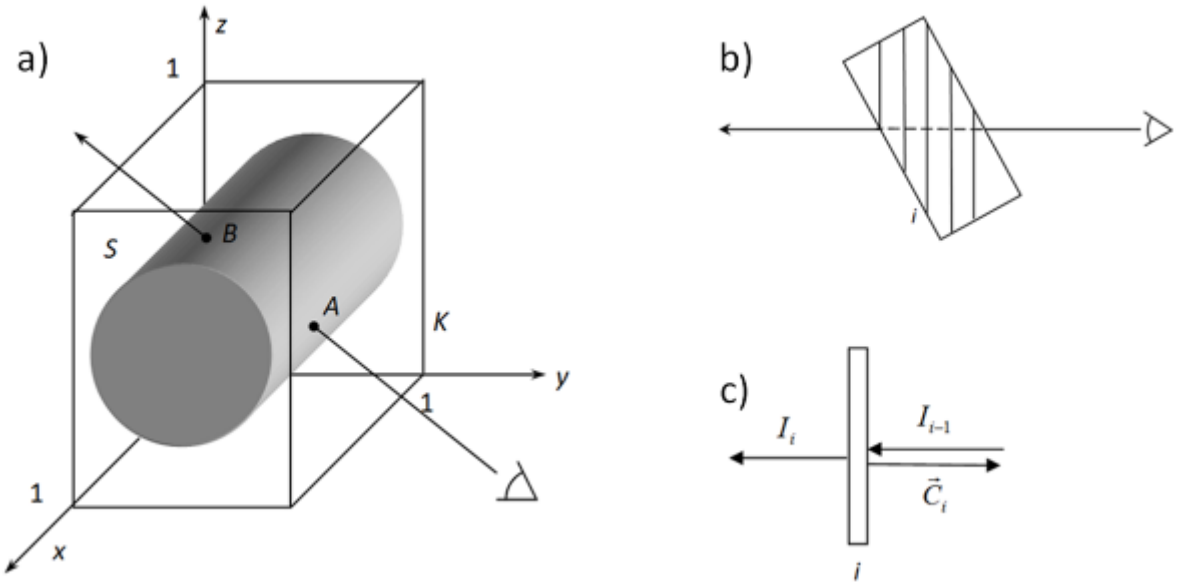

Fig. 3. Algorithm for visualization of three dimensional functions: a) texture map; b) division of the map into layers; c) influence of a map's layer on the beam.

We next consider how the beam penetrates through *n* layers. After passing through the *i*th layer, the beam intensity is equal to $I_i = (1 - \eta(f_i))I_{i-1}$, where $I_o = 1$, f_i is the value of the function in the *i*th layer and $\eta(f_i)$ is the transfer function. This function is specified by the user and maps the values of the function being visualized into the virtual medium density.

The color of each layer is determined by the vector transfer function $\vec{\chi}(f_i)$, which is also specified by the user and is used for pseudocoloring, so that the contribution made by the *i*th point to the resulting color of the beam is $\vec{c}_i = I_{i-1}\eta(f_i)\vec{\chi}(f_i)$. To determine the total beam color change according to the function being visualized, it is assumed that the medium regions through which the beam passes do not act as consecutive color filters and that the system lacks multiple deflection, reflection and other effects. Thus, the beam color at the *i*th step is obtained by a simple summation of the influence of the *i*th point and the beam color in the previous step. The quantities I_n and $\vec{C}_n$ are the values of the resulting intensity and color of the beam.

This algorithm was calculated using a special module, VOXEL. The module is operated from a graphical user interface and includes subprograms for digital filtering and for rendering by backward ray tracing. Fig. 4 shows the work window for specifying 3D data, transfer functions $\eta(f_i)$ и $\vec{\chi}(f_i)$ and other parameters.

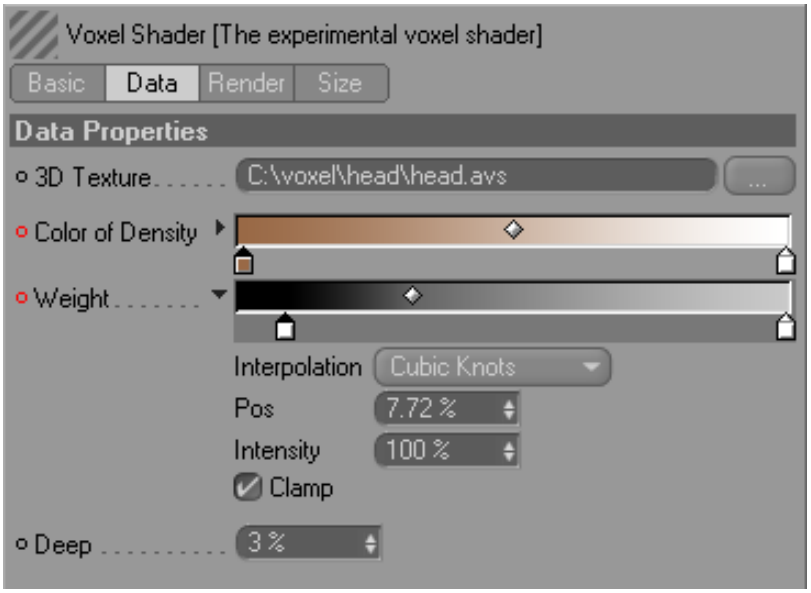

Fig. 4. Graphic interface for VOXEL modulus where transfer functions can be specified. Weight – $\eta(f_i)$, transfer function for intensity. Color of density – $\vec{\chi}(f_i)$, transfer function for pseudocoloring;

Varying the transfer functions enables the user to display the various details of a tomogram. Thus, in order to provide a general view of a tomogram, the transfer-function parameters were chosen as follows. The pseudocoloring scale (Density Color) was determined as a uniform color gradient; here, brown was assigned to the regions of the tomogram with minimum density and white was assigned to the regions with maximum density. The scale of intensity (Weight) was also specified as a uniform monochromatic gradient in which black color (and accordingly, maximum transparency) corresponded to the regions with minimum density. It should be noted that here the maximally transparent regions began at 7.72% of the overall tomogram density. This expedient assigns a maximum degree of transparency to the regions with densities of 0% to 7.72%, concealing them from the viewer and so serving as a noise cut off. A light-gray color and high opacity level corresponded to the regions with maximum density. As a result, the head shape of the experimental subject can be visualized as a basis for the virtual scene of the experiment (Fig. 5). Choosing other parameters for the transfer functions allows visualization of the brain's internal structure and the positions of the current dipoles.

Technique of synchronous dynamic visualization of dissimilar data

Construction of the 3D scenes and computation of the animated sequences was performed with the Cinema 4D software system [17, 18]. Integrated dynamic visualization of the output signals from all the magnetic-encephalograph sensors and from the complex spatial-temporal function was performed in the Digital Fusion v.4.04c environment [19, 20]. The movie consists of three episodes that describe the main steps of obtaining and analyzing the magnetic-encephalography and NMR tomography data.

Episode 1 describes the appearance of the subject's head and the arrangement of the magnetic encephalograph sensors. This episode shows the integration of data obtained in different experiments in an integrated virtual space. Information on the head's anatomic structure was obtained by magnetoresonance tomography, while the spatial arrangement of the sensors was determined in the course of a magnetic-encephalography experiment using reference coils placed at three reference points (the nasion and the left and right preauricular points). A relation between the two coordinate systems of the two experiments was established using contrast marks placed at reference points that can be clearly seen on the tomogram.

Knowing the coordinates of the magnetometers and using the features of the Cinema 4D software, we constructed a low-polygonal helmet-shaped surface on which the normal component of the magnetic field was measured. The experimental maps of the magnetic fields obtained in the MRIAN environment were then superimposed onto this surface [4, 5]. It should be noted that, in the first episode, we present only static data; here, the object motion was realized only for viewing convenience.

Episode 2 presents a synchronous picture of dissimilar experimental data. Among these is a graph of an auditory stimulus that was tentatively voiced during its input. Experimental magnetoencephalograms are presented alongside the graph from all 148 registration channels, and the marker indicates the time duration. The magnetic-field maps formed by the sensor readings are also displayed; the use of two panels makes it possible to visualize the maps as viewed from two different points. On these maps, the light blue and blue colors correspond to the direction of magnetic-force lines into the head, while yellow and red correspond to lines out of the head. All the data were imported into the Digital Fusion software package, where the algorithmic network (Fig. 7) brought the graphs into coincidence with a unified scale and the time marker was synchronized with the field map. Fig. 8 shows an integrated picture of the magnetic-field pattern and time series for all of the registration channels.

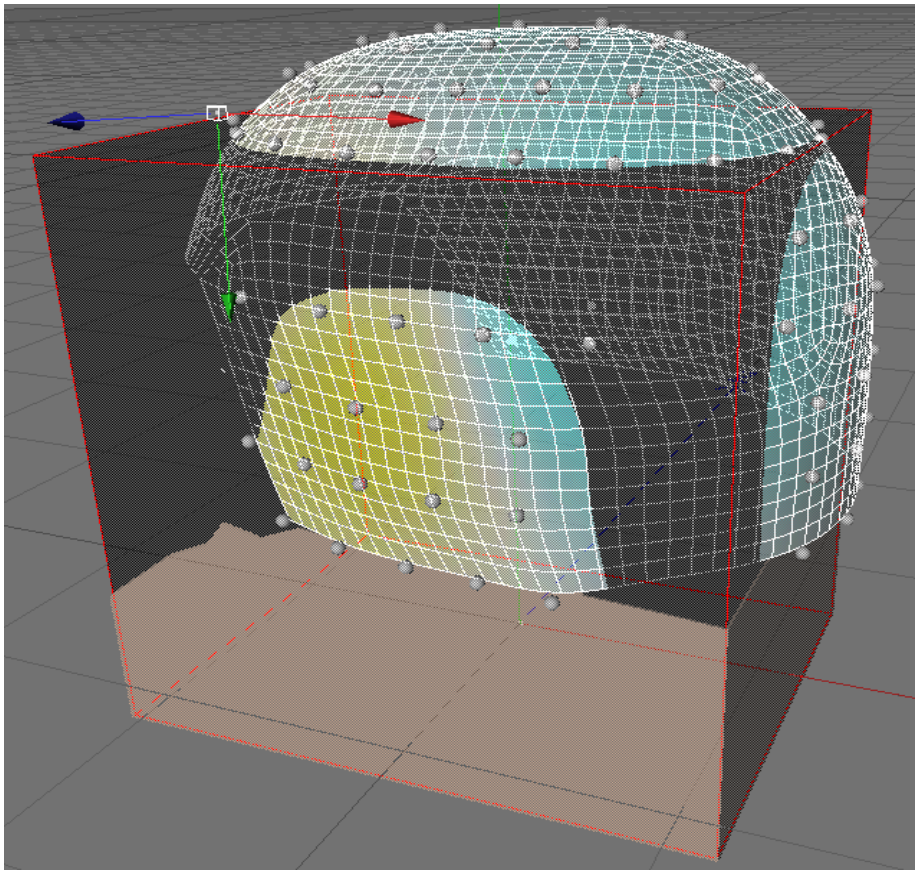

Fig. 5. Construction of 3D scene for integrated displaying of the tomogram (rectangular container sketched by red lines), arrangement of sensors in space (grey spheres) and a helmet with the magnetic field map.

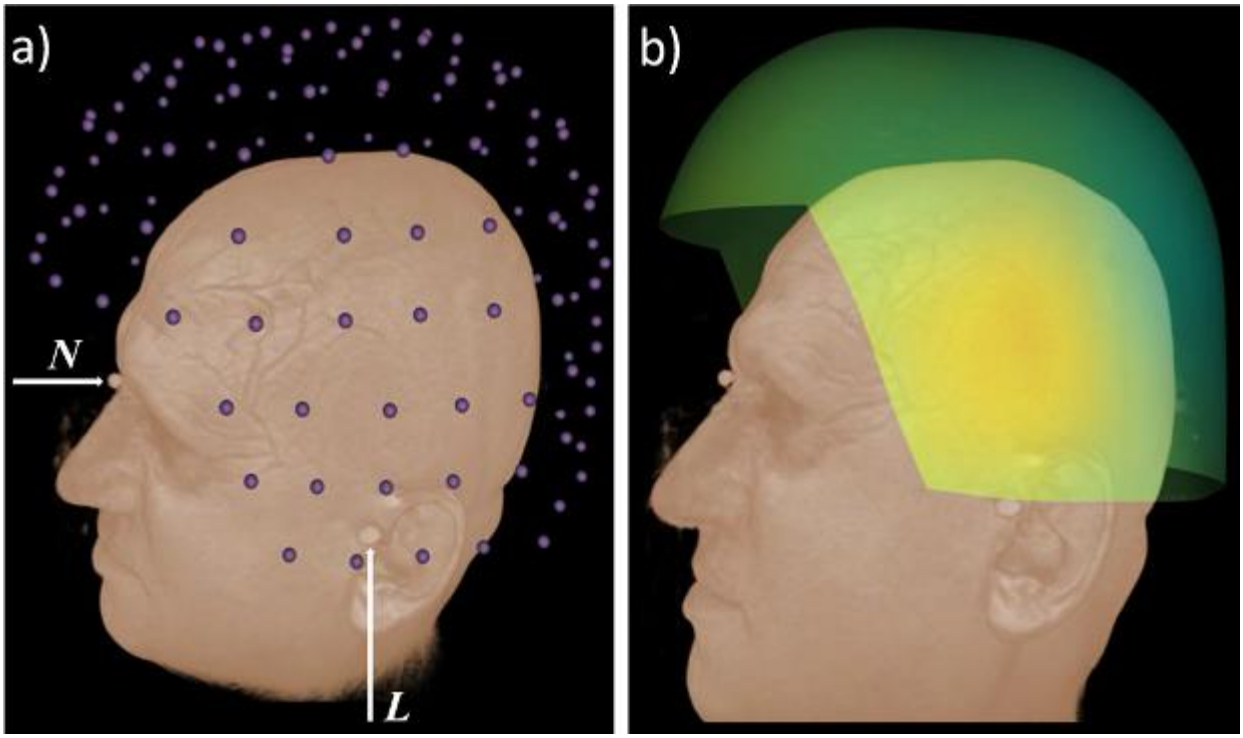

Fig. 6. Fragments of episode 1. a) Arrangement of the magnetic encephalograph sensors in the 3D space over the subject's head. Two reference points are shown: ***N*** – nasion, ***L*** – left preauricular point; b) Surface for demonstration of the magnetic field maps constructed from the sensors' coordinates.

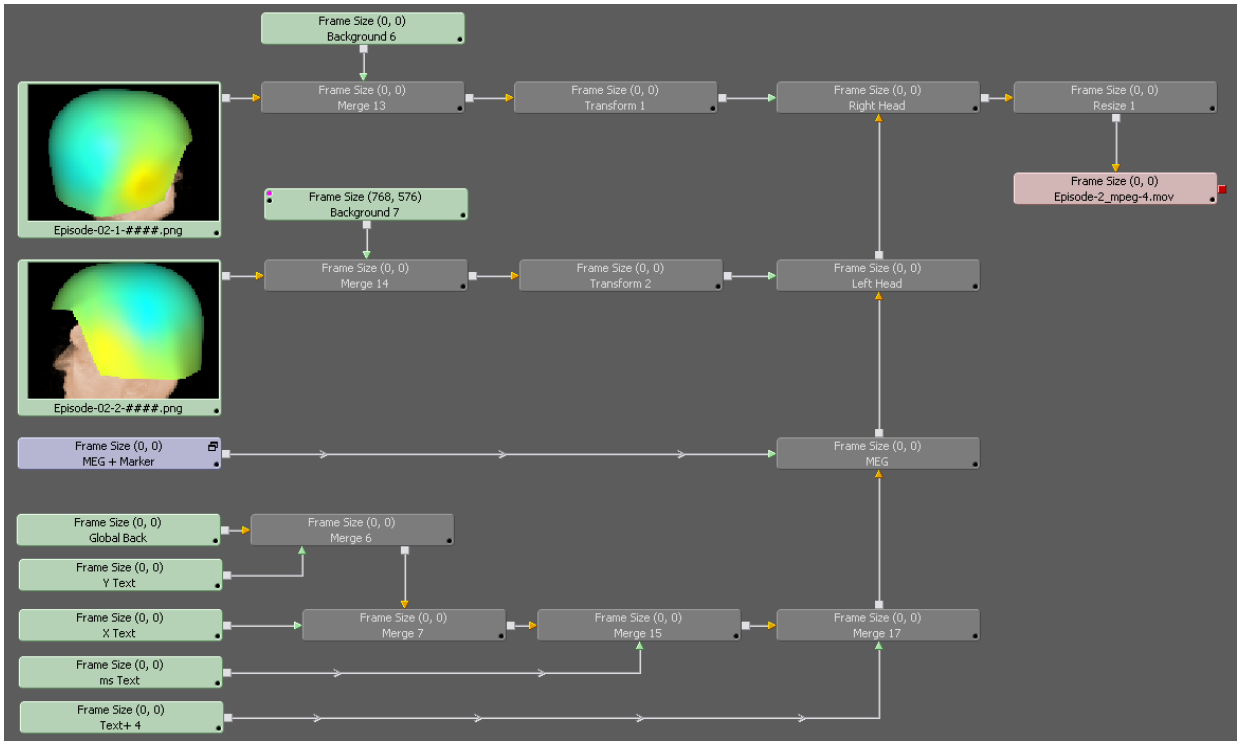

Fig. 7. Algorithmic network for integrated displaying of the graphs of output signals from the magnetic encephalograph sensors and the magnetic field's dynamic maps superimposed on the registration surface.

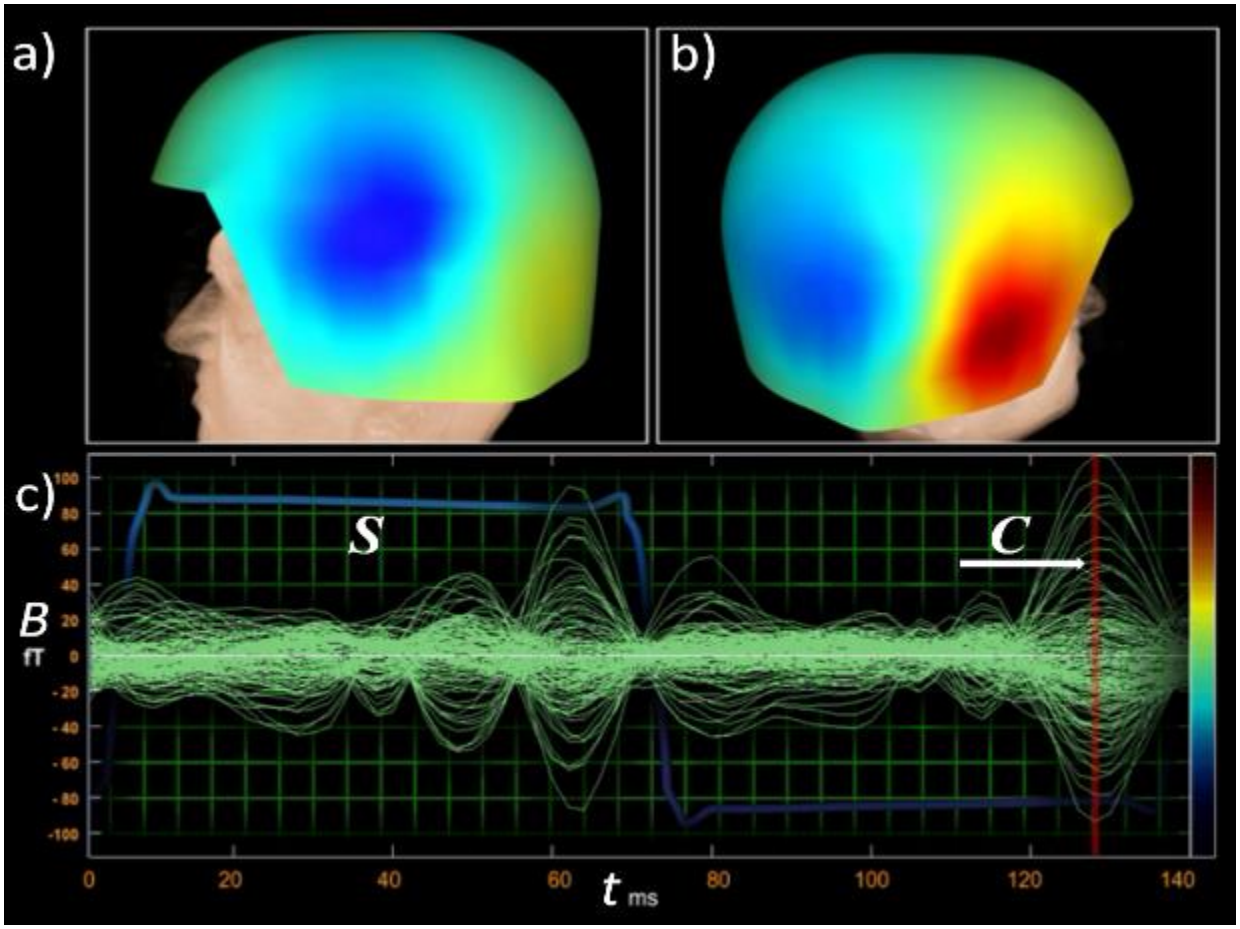

Fig. 8. Fragment of episode 2. Experimental data and mapping of the magnetic field. a) magnetic field map, left-side view; b) magnetic field map, right-side view; c) time dependence of the readings of all 148 magnetoencephalograph channels, stimulus amplitude (***S***), moving time marker (***C***).

Episode 3 presents a synchronous dynamic visualization of both the positions and orientations of equivalent current dipoles on the head tomogram and the magnetic-field patterns. Polygonal pointers were created to illustrate the directions of the dipoles. Their coordinates were determined from the solution of the magnetic encephalography inverse problem for the model of two current dipoles and rendered onto the virtual space of the scene. These coordinates correspond to the auditory centers of the cortex. To visualize dipoles on the tomogram, we used the graphical interface of the VOXEL program and chose the transfer-function parameters so as to render the external hard-textured layers of the tomogram invisible. This mode of visualization enabled us to present the internal structure of the brain as a three-dimensional medium and visualize the current dipoles as objects of varying brightness. The presentations of the magnetic encephalograms, along with the positions and strengths of the dipoles, were synchronized using an algorithmic network similar to that shown in Fig. 7.

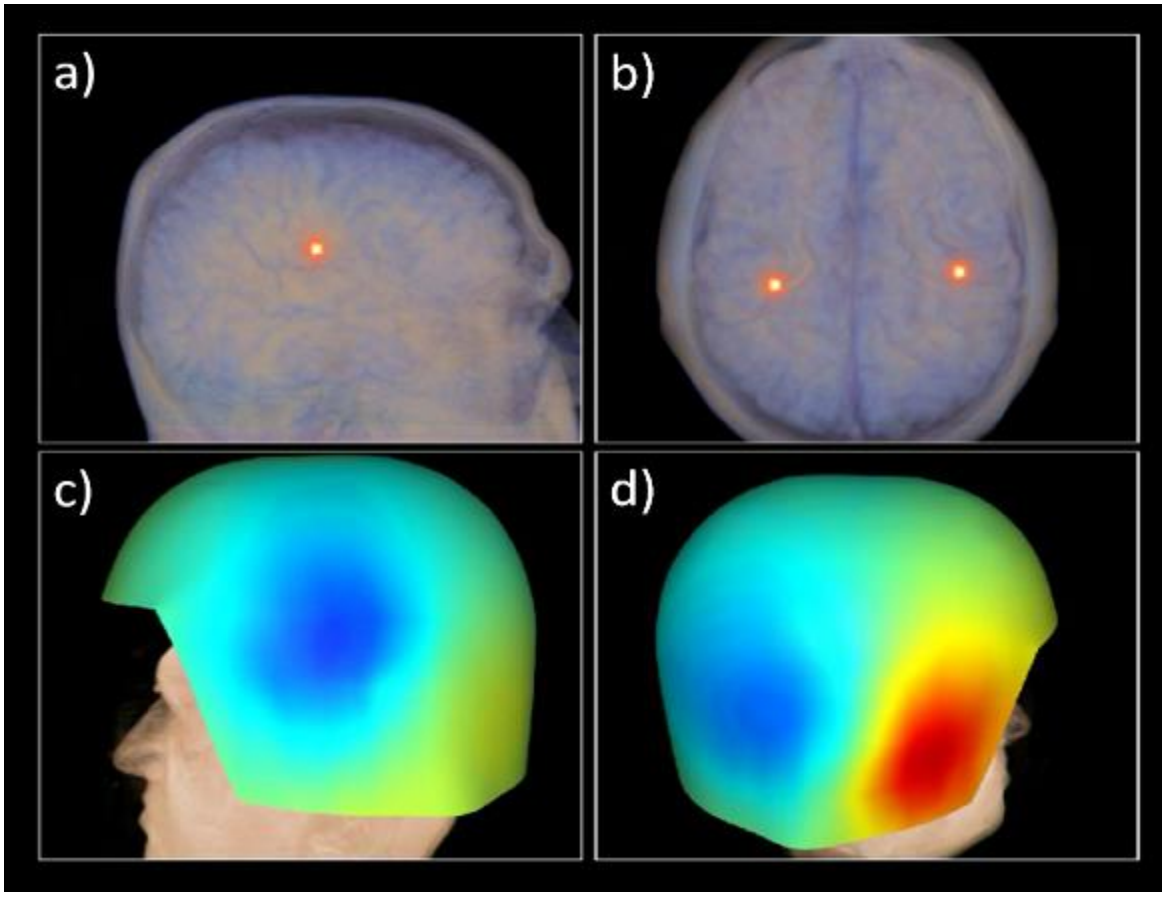

Fig. 9. Fragment of episode 3. Experimental magnetic field patterns and solution of the inverse problem: a) side view of the brain's internal structure and position of dipoles for the field shown below; b) top of the brain's internal structure and position of dipoles for the field shown below; c) magnetic field map, left-side view; d) magnetic field map, right-side view.

CONCLUSIONS

The magnetic-encephalography data from an auditory experiment were analyzed. The sequence of magnetic-field patterns (corresponding to brain activity) was evoked by periodic stimulus and then extracted. For each pattern, the coordinates and moments of two current dipoles were evaluated.

We developed a software system to present the complicated 3D data. Using this software and other visualization methods, we constructed dynamic 3D scenes displaying the experimental objects: the brain, the measuring equipment, the experimental setup, the experimental data and the data-processing results. As a result, a 69-s computer movie was produced, with a 25-fps frame rate and a resolution of 768 × 576 pixels. This movie illustrates both the magnetic-encephalography method in general and the particular experiment described herein. The methods and software developed here can be used for the visualization of other complicated experiments.

The work was partly supported by the American Foundation of Civil Research and Development (project CRDF RB1-2027), the Russian Foundation for Basic Research (projects 09-07-12108 and 10-07-00300), and by the Russian Federal Contract № 02.512.12.2049.

REFERENCES

1. Llinas R., Ribary U., Jeanmonod D., Kronberg E., Mitra P. Thalamocortical dysrhythmia: A neurological and neuropsychiatric syndrome characterized by

magnetoencephalography. *Proceedings of the National Academy of Sciences of the United States of America*. 1999. V. 96. P. 15222–15227.
2. Carver F.W., Fuchs A., Jantzen K.J., Kelso J.A.S. Spatiotemporal analysis of the neuromagnetic response to rhythmic auditory stimulation: rate dependence and transient to steady-state transition. *Clinical Neurophysiology*. 2002. V. 113. P. 1921–1931.
3. Mikhailova E.S., Slavutskaya A.V., Konyshev V.A., Pirogov Yu.A., Anisimov N.V., Shevelev I.A. Location of the Dipoles of the P1 Wave of Visual Evoked Potential in the Human Brain. *Doklady Biological Sciences.* 2006. V. 409. P. 285–289.
4. Ustinin M.N., Makhortykh S.A., Molchanov A.M., Ol'shevetz M.M., Pankratov A.N., Pankratova N.M., Sukharev V.I., Sychev V.V. Problems of magnetic encephalography data analysis. In: *Computers and supercomputers in biology*. Eds. Lakhno V.D. and Ustinin M.N. Moscow-Izhevsk: Institute of computer research, 2002. P. 327–348 (In Russian).
5. Ustinin M.N. *Spectral-analytic methods of computational and experimental data processing*. Doctor thesis of physical and mathematical sciences. Pushchino. 2004 (In Russian).
6. Lü Z.L., Williamson S.J., Kaufman L. Human auditory primary and association cortex have differing lifetimes for activation traces. *Brain Res*. 1992. V. 572. P. 236–241.
7. Sarvas J. Basic mathematic and electromagnetic concepts of the biomagnetic inverse problem. *Phys. Med. Biol.* 1987. V. 32. P. 11–22.
8. Lagarias J.C., Reeds J.A., Wright M.H., and Wright P.E. Convergence properties of the Nelder-Mead simplex method in low dimensions. *SIAM Journal of Optimization. 1998.* V. 9. P. 112–147.
9. Sandwell D.T. Biharmonic spline interpolation of GEOS-3 and SEASAT altimeter data. *Geophysical Research Letters*. 1987. V. 2. P. 139–142.
10. Herman G.T. and Liu H.K. Three-Dimensional Display of Human Organs from Computer Tomograms. *Computer Graphics and Image Processing*. 1979. V. 9. № 1. P. 1–21.
11. Pizer S.M., Fuchs H., Mosher C., Lifshitz L., Abram G.D., Ramanathan S., Whitney B.T., Rosenman J.G., Staab E.V., Chaney E.L. and Sherouse G. 3-D Shaded Graphics in Radiotherapy and Diagnostic Imaging. *NCGA'86 conference proceedings*. Anaheim, CA. 1986. P. 107–113.
12. Lorensen W.E., Cline H.E. Marching Cubes: A High Resolution 3D Surface Construction Algorithm. *Computer Graphics.* 1987. V. 21. № 4.
13. Cabral B., Cam N. and Foran J. Accelerated Volume Rendering and Tomographic Reconstruction Using Texture Mapping Hardware. *ACM Symp. on Vol. Vis.* 1994.
14. Levoy M. Display of Surfaces from Volume Data. *IEEE Computer Graphics and Applications*. 1988. V. 8. № 3. P. 29–37.
15. Drebin R.A., Carpenter L. and Hanrahan P. Volume Rendering. *SIGGRAPH Comput. Graph*. 1988. V. 22. P. 65–74.
16. Sobolev.E.V. Dynamical visualization of 3D data of biological experiments: Master's thesis in applied mathematics. Pushchino, 2003. (In Russian).
17. Maxon. Cinema 4D. URL: www.maxon.net
18. URL: http://www.pcpro.co.uk/reviews/software/250669/maxon-cinema-4d-11
19. Eyeon. Digital Fusion. URL: www.eyeonline.com
20. URL: http://www.eyeonline.com/Web/EyeonWeb/Products/fusion6/fusion6.aspx

Received December 10, 2010.
Published December 14, 2010.